processes

MDPI

Article

CFD–DEM Investigation of Heat Transfer and Flow Characteristics in a Fluidized Bed Under Van Der Waals Forces Effects

Lei Wang [1,*], Junnan Liu [2] and Hongwu Qin [1]

[1] College of Electronic and Information Engineering, Changchun University, Jilin 130022, China
[2] Jilin Green Energy Industry Service Center, Jilin 130021, China
* Correspondence: wangl94@ccu.edu.cn

Abstract

Particle cohesion induced by van der Waals (VDW) forces can substantially affect the fluidization and heat-transfer behavior of fine polyethylene particles in gas–phase fluidized bed reactors, particularly under industrially relevant high temperature and high pressure. In this study, a computational fluid dynamics discrete-element method (CFD–DEM) model incorporating VDW forces and heat transfer is developed. This model is utilized to investigate particle-scale hydrodynamics and thermal behavior under high temperature and high pressure. Simulations with and without VDW forces are compared at inlet gas velocities of 0.012 and 0.020 m/s. The results show that VDW forces redistribute local gas volume fraction states and enhance particle connectivity, with elevated coordination numbers preferentially observed near the sidewalls and bottom corners. The influence of these interactions on particle transport becomes more evident at the higher gas velocity. VDW forces have a limited effect on the overall axial gas temperature distribution because the gas rapidly approaches the particle temperature near the inlet. In contrast, the influence on particle-gas convective heat transfer is more pronounced at an inlet gas velocity of 0.020 m/s, increasing the average heat-transfer coefficient by up to 6.12%. This study reveals the gas-velocity-dependent effects of cohesive forces caused by VDW forces on particle transport and heat transfer in polyethylene fluidized bed reactors.

Keywords: fluidized bed reactor; CFD–DEM; van der Waals forces; high temperature and high pressure; heat transfer and flow characteristics

Check for updates

Academic Editor: Marco Ramírez-Argáez

Received: 13 September 2026
Revised: 15 October 2026
Accepted: 21 October 2026
Published: 23 October 2026

Copyright: © 2026 by the authors. Licensee MDPI, Basel, Switzerland. This article is an open access article distributed under the terms and conditions of the Creative Commons Attribution (CC BY) license.

1. Introduction

The fluidized bed reactors are widely used in the industrial production of polyethylene owing to their excellent heat and mass transfer performance, high production capacity, and operational flexibility [1,2]. During polyethylene production in fluidized bed reactors, however, particles undergo continuous motion, collision, and friction, leading to complex interparticle interactions. Under certain operating conditions, attractive forces, such as electrostatic and van der Waals (VDW) forces, can promote particle adhesion and consequently induce agglomeration [3,4]. The formation of particle agglomerates can substantially alter the hydrodynamic behavior, heat and mass transfer, and polymerization characteristics within the reactor, thereby affecting the stability and efficiency of the polymerization process [5]. Therefore, a comprehensive understanding of particle interactions and flow behavior in fluidized bed reactors is essential for optimizing reac-

tor design, improving operational stability, and mitigating particle agglomeration during polyethylene production.

Among the various polyethylene production technologies, gas-phase polymerization has attracted considerable attention because of its relatively simple process configuration, high reactor productivity, and absence of a liquid diluent [6]. To better understand the polymerization process and multiphase flow behavior in gas-phase polyethylene fluidized bed reactors, a variety of mathematical and numerical models have been developed. These include the population balance model (PBM) [7–10], the multi compartment PBM [11], the coupled Euler–Euler two fluid model and PBM [12], the Lagrangian–Eulerian hybrid model [13], and a gas–solid–liquid three-fluid computational fluid dynamics (CFD) model incorporating both PBM and liquid evaporation models [14]. These modeling approaches have provided valuable insights into polymerization kinetics, particle size distribution, and gas–solid flow characteristics in fluidized bed reactors. In particular, the coexistence of emulsion and bubbling phases plays an important role in determining the local flow and reaction characteristics, as polymerization may occur in both phases under practical operating conditions.

In addition to gas–solid hydrodynamics and polymerization kinetics, interparticle and particle–wall interactions are critical to the formation and evolution of agglomerates in polyethylene fluidized bed reactors. Frequent particle–particle collisions generate interaction forces that may promote particle adhesion and agglomeration, while repeated particle–wall collisions may cause sticky particles to adhere to the reactor wall, potentially resulting in wall sheeting. Several studies have suggested that electrostatic interactions are an important factor contributing to particle agglomeration and wall sheeting [15–19]. However, Briens et al. [20] investigated the flow behavior of polyethylene particles with a diameter of 400 μm and concluded that electrostatic interactions were unlikely to be the primary cause of agglomerate formation. In contrast, Zhang et al. [21] experimentally observed particle adhesion to the reactor wall and elucidated the corresponding adhesion mechanism. The results suggested that monopolar-charged particles could adhere to the wall through the combined effects of the electric field generated by the wall and VDW forces. Jiang et al. [22] theoretically analyzed the electrostatic forces acting on polyethylene particles and compared them with gravitational and VDW forces over a range of particle sizes. The results demonstrated that the VDW forces exceeded the electrostatic force for particles smaller than 150 μm, highlighting the potentially dominant role of VDW forces interaction for fine particles.

The importance of VDW forces in gas–solid fluidization has also been demonstrated by numerous numerical and experimental studies. Visser [23] proposed that VDW forces constitute a major attractive force between particles in fluidized beds and may also contribute significantly to particle–wall adhesion. Li et al. [24] investigated Geldart A particles by comparing simulated bubble size and velocity with experimental measurements and demonstrated that accounting for VDW forces interaction was necessary to accurately reproduce bubble morphology and solids circulation. Shrestha et al. [25] further examined the effects of VDW forces and particle geometry on bubble dynamics during gas fluidization using a coupled CFD–DEM approach. The results showed that increasing the strength of VDW forces interaction could induce a transition from conventional bubbling fluidization to a non-bubbling regime for nonspherical particles, whereas channeling behavior was observed for spherical particles. Gu et al. [26] investigated the gas fluidization of Geldart. CFD–DEM is used to simulate particles subject to VDW forces. By varying the particle spring stiffness, it was found that particle hardness had a limited influence on the overall bubble distribution. Mihajlovic et al. [27] developed a DEM-based approach to investigate the effects of different interparticle interactions on fluidization behavior and proposed

a physically consistent numerical treatment for calculating VDW forces during particle contact. Collectively, these studies demonstrate that VDW forces can substantially modify particle scale dynamics and macroscopic fluidization behavior, particularly in cohesive particulate systems.

Despite these advances, the coupled effects of VDW forces on the hydrodynamic and heat-transfer characteristics of fine polyethylene particles under industrially relevant high temperature and high pressure remain insufficiently understood. In particular, the effect of VDW forces on particle connectivity, local gas–solid flow structures, and particle-gas heat transfer at different gas velocities has received limited attention.

In the study, a coupled CFD–DEM model incorporating VDW forces and heat transfer is employed to investigate the fluidization behavior of fine polyethylene particles under high temperature and high pressure. Simulations with and without VDW forces are systematically compared at two inlet gas velocities. The effects of VDW forces are quantified in terms of the gas volume fraction, coordination number, interparticle VDW forces, particle velocity, gas temperature, and gas–solid heat transfer coefficient. Particular attention is devoted to the gas-velocity-dependent influence of VDW forces on particle connectivity and transport, local gas–solid flow structure, and convective heat transfer. This study provides particle-scale insight into the coupling between cohesive interactions, fluidization dynamics, and heat transfer in polyethylene fluidized bed reactors, with implications for understanding and controlling cohesive particle behavior under practical operating conditions.

2. Governing Equations

In the present CFD–DEM framework, the continuous gas phase is solved in a Eulerian framework, whereas each solid particle is tracked individually in a Lagrangian framework. Momentum and energy are exchanged between the two phases through gas-particle drag and convective heat transfer. This two-way coupling enables the effects of particle-scale interactions, including collisions and van der Waals forces, to be linked to the gas-phase flow and temperature fields. The governing equations and interaction models are briefly introduced below [28,29].

2.1. Governing Equations of Solid Phase

Newton's second law is used to calculate the motion of each particle:

$$m_i \frac{d\mathbf{v}_i}{dt} = \mathbf{F}_{p,i} + \mathbf{F}_{d,i} + \sum_{j=1}^{N_j} \mathbf{F}_{c,ij} + \sum_{k=1}^{N_k} \mathbf{F}_{VDW,ik} + m_i \mathbf{g} \tag{1}$$

where $\mathbf{v}_i$ is the particle translational velocity, $\boldsymbol{F}_{p,i}$ is the pressure gradient force, $\mathbf{F}_{d,i}$ is the drag force, $\mathbf{F}_{c,ij}$ is the contact force, and $\mathbf{F}_{VDW,ik}$ is the inter particle VDW forces.

The angular momentum of particle i is given by the following equation:

$$I_i \frac{d\boldsymbol{\omega}_i}{dt} = \mathbf{M}_i \tag{2}$$

where I_i is the moment of inertia, $\boldsymbol{\omega}_i$ is the angular velocity, and $\mathbf{M}_i$ is the torque.

Hamaker [30] derived the VDW forces equation between two spheres:

$$\mathbf{F}_{VDW} = \frac{\mathrm{A}}{3} \frac{2r_i r_k (S + r_i + r_k)}{[S(S + 2r_i + 2r_k)]^2} \left[\frac{S(S + 2r_i + 2r_k)}{(S + r_i + r_k)^2 - (r_i - r_k)^2} - 1 \right]^2 \mathbf{n} \tag{3}$$

where S is the distance between the sphere surfaces, A is the Hamaker constant, and r is the sphere radius.

The minimum cut-off separation distance $S_{\min}$ = 1 nm is set to prevent dispersion upon particle collision [25,31]. Since the VDW forces decreases rapidly with increasing separation, a maximum cut-off separation distance $S_{\max} = (r_i + r_k)/4$ [26,32] is utilized to speed up the simulation, beyond which the VDW forces are neglected. The VDW forces between two spheres i, k has a certain distance h of action. When $S < S_{\min}$, $h = r_i + r_k + S_{\min}$; when $S_{\min} < S < S_{\max}$, $h = r_i + r_k + S$; when $S > S_{\max}$, $h = 0$. For separation distances much smaller than the particle radius, the van der Waals force is approximately proportional to A/S^2. Thus, the force varies linearly with the Hamaker constant and inversely with the square of the minimum separation distance. A larger Hamaker constant or a smaller minimum separation distance produces stronger cohesive interactions and may promote particle contacts and agglomeration. Therefore, the quantitative results reported in this study apply to the selected values.

Since both dilute and dense phase regions coexist in the fluidized bed, the Gidaspow drag model is selected to calculate the drag force [33,34]. The Hertz–Mindlin contact model is utilized to simulate the particle-to-particle and particle-to-wall contact forces [35].

2.2. Governing Equations of Gas Phase

The continuity equation and the Navier–Stokes equation are used to describe the gas-phase motion.

$$\frac{\partial}{\partial t}(\varepsilon_g \rho_g) + \nabla \cdot (\varepsilon_g \rho_g \mathbf{u}_g) = 0 \tag{4}$$

$$\frac{\partial}{\partial t}(\varepsilon_g \rho_g \mathbf{u}_g) + \nabla \cdot (\varepsilon_g \rho_g \mathbf{u}_g \mathbf{u}_g) = -\varepsilon_g \nabla p_g - \nabla \cdot (\varepsilon_g \boldsymbol{\tau}_g) - \mathbf{S}_i + \varepsilon_g \rho_g \mathbf{g} \tag{5}$$

where ε_g is the gas-phase local porosity, ρ_g is the density, p_g is the pressure, $\mathbf{u}_g$ is the velocity, $\boldsymbol{\tau}_g$ is the stress tensor of gas-phase, and $\mathbf{S}_i$ is the volumetric particle to gas interaction force.

2.3. Heat-Transfer Model

Particle-energy-control equations are given by:

$$m_i c_i \frac{dT_i}{dt} = \sum_{j=1}^{k_c} Q_{ij} + Q_{i,g} \tag{6}$$

where c_i, T_i are the heat capacity and temperature of particles respectively, Q_{ij}, $Q_{i,g}$ are the heat transfer between particles, and the convective heat exchange between particles and gas, k_c is an amount of particles in contact with particle i where heat transfer occurs.

Two types of heat conduction are present between particles. One is static-contact heat transfer when zero is the relative velocity. The other is collisional heat transfer when the particles have relative velocity [36].

Static-contact heat transfer:

$$Q_{ij} = \frac{4r_c(T_i - T_j)}{1/\lambda_i + 1/\lambda_j} \tag{7}$$

Collisional heat transfer:

$$Q_{ij} = \frac{\delta(T_i - T_j)\pi r_c^2 t_c^{-1/2}}{(\rho_i c_i \lambda_i)^{-1/2} + (\rho_j c_j \lambda_j)^{-1/2}} \tag{8}$$

where λ, r_c, t_c, ρ, T are the thermal conductivity, contact radius, collision time, particle density, and temperature, respectively, and δ is the correction factor.

The convective heat transfer between particle i and the gas is [37,38]:

$$Q_{i,g} = h_i A_i (T_i - T_g) \tag{9}$$

where A_i is particle external surface area, T_g is gas temperature, and h_i is convective heat transfer coefficient (HTC) on particle surfaces:

$$h_i = \frac{Nu\lambda_g}{d_i} \tag{10}$$

where λ_g is the gas thermal conductivity.

3. Simulation Models

3.1. Simulation Conditions

Figure 1a schematically illustrates the polyethylene production process. In the gas-phase fluidized bed polymerization process, an ethylene-containing gas mixture is continuously introduced into the fluidized bed reactor, which is initially charged with fine catalyst particles. The reactor is typically operated at a pressure below 2.4 MPa and a temperature ranging from 353 to 373 K. The heat generated during polymerization is removed by a cooling and condensing gas stream, while the cooled gas and condensed liquid are subsequently recycled to the reactor. Polyethylene particles produced during polymerization are discharged intermittently, resulting in a finite particle-residence time within the reactor. During this process, frequent particle–particle and particle–wall interactions can lead to particle adhesion and agglomeration, which may significantly affect particle motion, hydrodynamics, and heat-transfer characteristics within the fluidized bed.

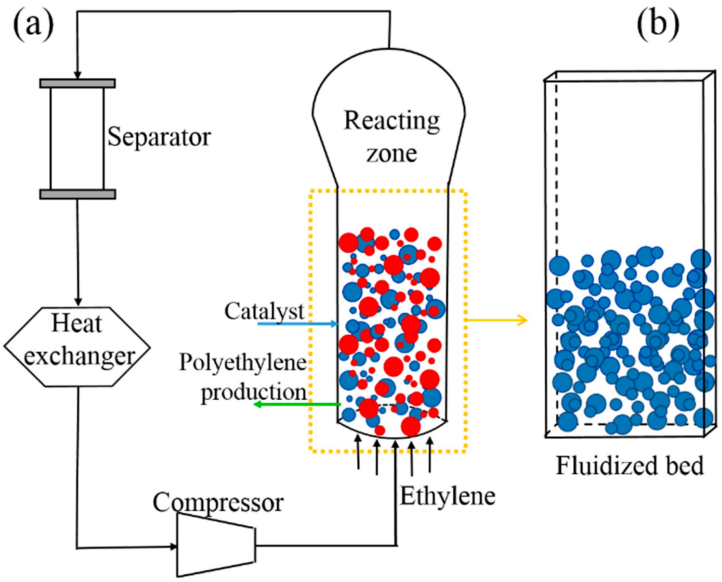


Figure 1. (**a**) Polyethylene production process and (**b**) computational domain.

To investigate the particle-scale effects of interparticle VDW forces on the flow and heat-transfer behavior of fine polyethylene particles, a reduced quasi-two-dimensional computational domain is employed, as shown in Figure 1b. The domain is not a geometrically scaled representation of the complete industrial reactor. Instead, it is designed to resolve individual particle motion, particle contacts, cohesive interactions, and particle-to-gas heat transfer under the specified temperature and pressure while maintaining a feasible computational cost. The domain dimensions are 3 mm × 0.18 mm × 7.65 mm. The thin depth produces a quasi-two-dimensional configuration that facilitates particle-scale

observation but also results in stronger wall confinement than that expected in an industrial reactor. Therefore, the simulations are used to compare the relative effects of including and excluding VDW forces under otherwise identical conditions, rather than to reproduce the complete industrial-scale hydrodynamics.

Geldart [39] classified fluidized particles into four groups (Geldart A, B, C, and D groups) according to the particle size and fluidization characteristics. Shabanian and Chaouki [40] reported that particles with diameters smaller than 100 μm are preferable for investigating the effects of VDW forces in fluidized beds. Accordingly, Geldart A particles are selected for the present study—specifically, polyethylene particles with diameters of 60 and 70 μm, which are first filled into the bed bottom under the influence of gravity. The corresponding operating and particle parameters employed in the simulations are summarized in Table 1.

Table 1. Simulation parameters.

Parameter	Value
Gas phase (ethylene mixture)	
Density, kg/m^3	20.2
Viscosity, Pa·s	1.72×10^{-5}
Specific heat capacity, J/(kg·K)	1416.4
Thermal conductivity, W/(m·K)	0.0282
Temperature, K	313
Solid phase (low density polyethylene)	
Diameter, μm	60/70
Number	2924/2148
Packing height, mm	2.5
Density, kg/m^3	918
Specific heat capacity, J/(kg·K)	2512.2
Thermal conductivity, W/(m·K)	0.025
Temperature, K	361
Hamaker constant, J [41]	2.1×10^{-21}
Minimum cut-off distance, nm	1
Young's modulus, Pa	3.0×10^7
Coefficient of restitution	0.98
Coefficient of static friction	0.3
Coefficient of rolling friction	0.01
Operating environment	
Pressure (MPa)	2
Temperature (K)	361
CFD mesh	$34 \times 2 \times 85$
Number of CFD cells	5780
Pressure-velocity coupling	Phase-Coupled SIMPLE
Turbulence model	Standard k-ε
Pressure discretization	Second order
Momentum discretization	First-order upwind
Turbulence discretization	First-order upwind
Energy discretization	Second-order upwind

During the simulations, a velocity-inlet boundary condition is imposed at the bottom of the reactor, while a pressure-outlet boundary condition is applied at the outlet. The fluidized bed reactor is operated at a pressure of 2 MPa and a temperature of 361. The ethylene-containing gas mixture is introduced through the bottom inlet. The computational domain is discretized into $34 \times 2 \times 85$ uniform hexahedral cells. For particle diameters

of 60–70 μm, the mesh-to-particle size ratio ranged from 1.26 to 1.50. The minimum cell dimension is larger than the maximum particle diameter. This mesh resolution is therefore considered suitable for the present unresolved CFD–DEM calculation. The transient gas-phase equations are solved using the phase-coupled SIMPLE algorithm. Second-order spatial discretization is applied to the pressure and energy equations, whereas first-order upwind discretization is used for the momentum, turbulent kinetic energy, and turbulent dissipation equations. The DEM and CFD time steps are 1.0×10^{-7} s and 2.0×10^{-6} s, respectively. The DEM time step corresponded to approximately 9.2–10.7% of the Rayleigh time, while the CFD time step produced a maximum inlet-based Courant number of 4.53×10^{-4}. The Courant number is substantially lower than unity. Each CFD time step contained 20 DEM substeps. These values satisfy the commonly adopted temporal-resolution criteria for CFD–DEM simulations. The solution at each time step is considered converged when the scaled residuals of the continuity, momentum, energy, turbulent kinetic energy, and turbulent dissipation equations decrease below 1×10^{-4}. The simulation data are recorded at 0.001 s intervals, and the total simulation time is 0.5 s.

3.2. Model Verification

3.2.1. Validation Against the Industrial Fluidized-Bed Reactor

The macroscopic predictions of the CFD–DEM model are assessed using the experimental pressure drop and temperature data reported for an industrial fluidized bed reactor [42]. These comparisons test the predicted bulk hydrodynamic and thermal behavior. They do not independently validate the magnitude of the interparticle VDW forces or the agglomeration behavior of the finer particles considered in the subsequent simulations. For the validation case, Geldart B particles with a diameter of 0.4 mm and a density of 918 kg/m^3 are employed to reproduce the particle characteristics under industrial operating conditions. According to the operating conditions of the industrial fluidized bed reactors, the inlet temperature of the gas phase is set to 356.6 K, while the outlet temperature is 360.6 K. The simulated and experimental results are compared in Figure 2, which presents the pressure drop and temperature distribution along the axial direction of the fluidized bed reactors.

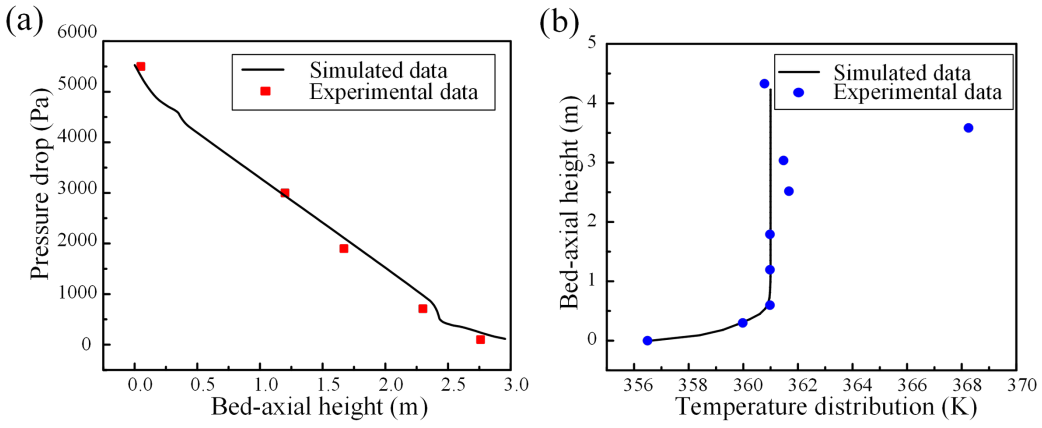


Figure 2. Comparison of simulation results with experiments of (**a**) pressure drop and (**b**) temperature along the bed-axial direction in a fluidized bed reactor.

In Figure 2a, the simulated pressure drop curve follows the measured decrease with bed height, although local discrepancies remain. Figure 2b indicates that the model captures the rapid temperature increase near the inlet and the temperature level of approximately 361 K over much of the bed. However, the measured temperature near a height of 3.6 m is approximately 368 K, whereas the simulation remains close to 361 K. This isolated peak may

be associated with local variations in solids holdup and gas–solid mixing, and wall heat-transfer effects not fully represented by the boundary conditions. Differences between the pointwise thermocouple measurements and the spatially averaged numerical temperature. Because the available experimental data do not permit these effects to be separated, the industrial comparison is interpreted as validation of the overall thermal trend rather than of the local temperature at every axial position.

3.2.2. Validation of the Cohesive-Particle Model

To assess the capability of the present CFD–DEM framework in describing the fluidization of fine cohesive particles, an additional validation is performed using the defluidization measurements of LaMarche et al. [43] for 69-μm soda-lime glass particles. Figure 3 compares the measured and predicted normalized bed-pressure drop during a stepwise decrease in superficial gas velocity.

$$\Delta P^* = \frac{\Delta P A_b}{W_b} \tag{11}$$

where ΔP^* is the pressure drop across the bed normalized by the bed weight (W_b) over the cross-sectional area (A_b) of the column.

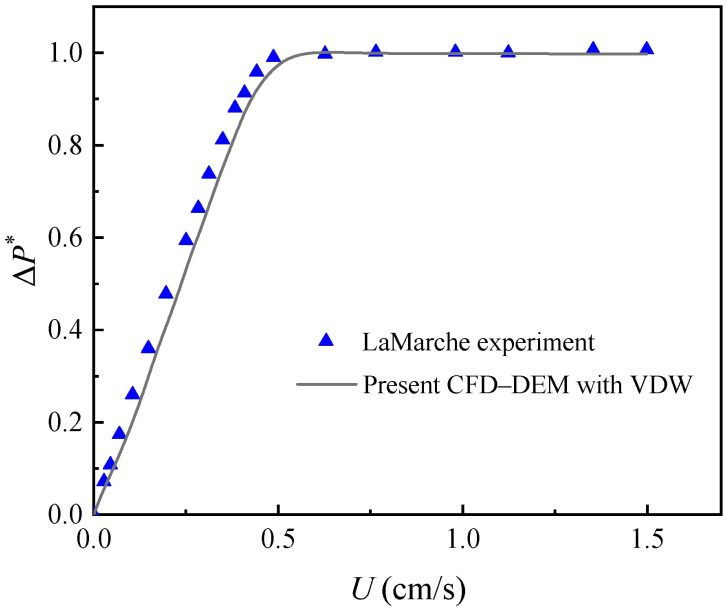


Figure 3. Experimental and CFD–DEM defluidization curves for 69-μm soda-lime glass particles.

At gas velocities above approximately 0.5 cm/s, both the experiment and simulation approach indicate that the particle weight is fully supported by the gas-phase drag. Moreover, the simulation reproduces the gradual nonlinear increase in pressure drop observed over the partially fluidized regime. This behavior results from the combined effects of interparticle cohesion, friction, particle rearrangement, and progressive transfer of the particle weight from the contact network to the gas phase. A small underprediction of the normalized pressure drop is observed at intermediate gas velocities of approximately 0.15–0.30 cm/s. This difference may be associated with the use of monodisperse particles and idealized boundary conditions in the simulation, as well as uncertainty in the experimental particle size and surface-roughness distributions. Nevertheless, the predicted curve captures both the shape of the partially fluidized regime and the fully fluidized pressure drop plateau. Using the criterion, the experimental and predicted complete fluidization velocities are approximately 0.47 and 0.50 cm/s, respectively, corresponding to a relative difference of approximately 6.4%. Together with the agreement in the overall shape of the

defluidization curve and the fully fluidized pressure-drop plateau, this result indicates that the model reasonably predicts the principal fluidization transition of the investigated fine cohesive particles.

4. Results and Discussion

4.1. Fluidized Dynamics

4.1.1. Gas-Volume Fraction Distribution

Figure 4 compares the probability distributions of the local gas-volume fraction at inlet gas velocities of 0.012 and 0.020 m/s. At 0.012 m/s, both cases exhibit a broad peak near a volume fraction of 0.52–0.55 and show an upward trend near a volume fraction of 1. Peaks at lower volume fractions represent regions with a relatively high concentration of particles, while values close to 1 represent nearly particle-free regions. At 0.020 m/s, the low-volume fraction peak is replaced by a broader, higher probability region located around 0.65–0.90, indicating that the probability distribution has shifted toward a more dilute local state.

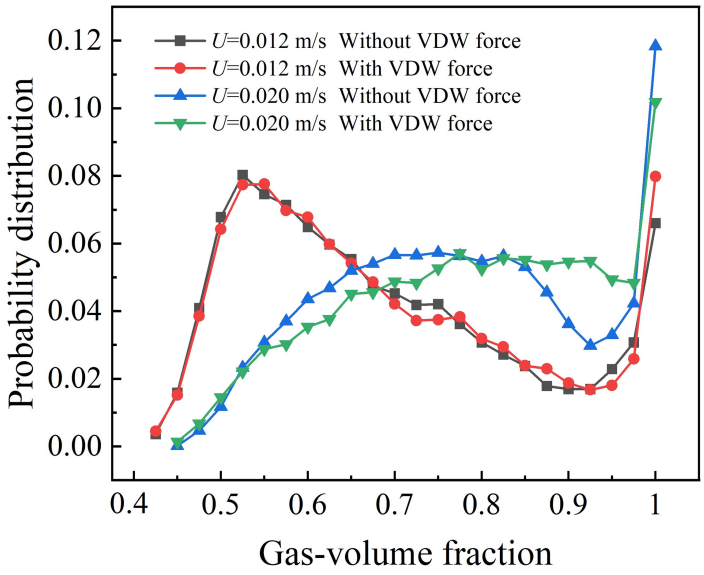


Figure 4. Probability distributions of gas volume fraction.

The influence of VDW forces depends on both the gas velocity and the gas-volume fraction. At a gas velocity of 0.012 m/s, the two probability distribution curves are nearly identical. However, at a gas-volume fraction of 1, incorporating VDW forces increases the probability from 0.065 to 0.080. At a higher gas velocity of 0.020 m/s, VDW forces increase the probability over the gas-volume fraction range of 0.88–0.97, whereas at a gas-volume fraction of 1, the probability decreases from 0.12 to 0.10. When VDW forces are neglected, the distribution exhibits a distinct local minimum at gas-volume fractions of approximately 0.92–0.95. This feature is substantially weakened when VDW forces are included. These results suggest that VDW forces redistribute probability within the dilute state regime rather than uniformly increasing the probability of the state with the highest gas volume fraction.

4.1.2. Coordination Number

The coordination number is the number of particles in direct contact with a given particle. Figures 5 and 6 present instantaneous coordination-number distributions and lateral profiles at 0.30 and 0.50 s. Both instants occur within the quasi-steady fluidization interval identified from the bed-pressure drop. These results are used to examine representative

instantaneous particle-contact structures. The differences between the two instants reflect the dynamic formation, movement, and disruption of cohesive contact networks during quasi-steady fluidization. Figure 5a,b correspond to 0.012 m/s without and with VDW forces, respectively. Figure 5c,d show the corresponding cases at 0.020 m/s. Most particles have a coordination number of zero, while localized regions with nonzero coordination number occur in all cases. Considering the effects of VDW forces, regions with higher coordination number values become more prominent, particularly near the side walls and bottom corners, which is consistent with increased local particle connectivity.

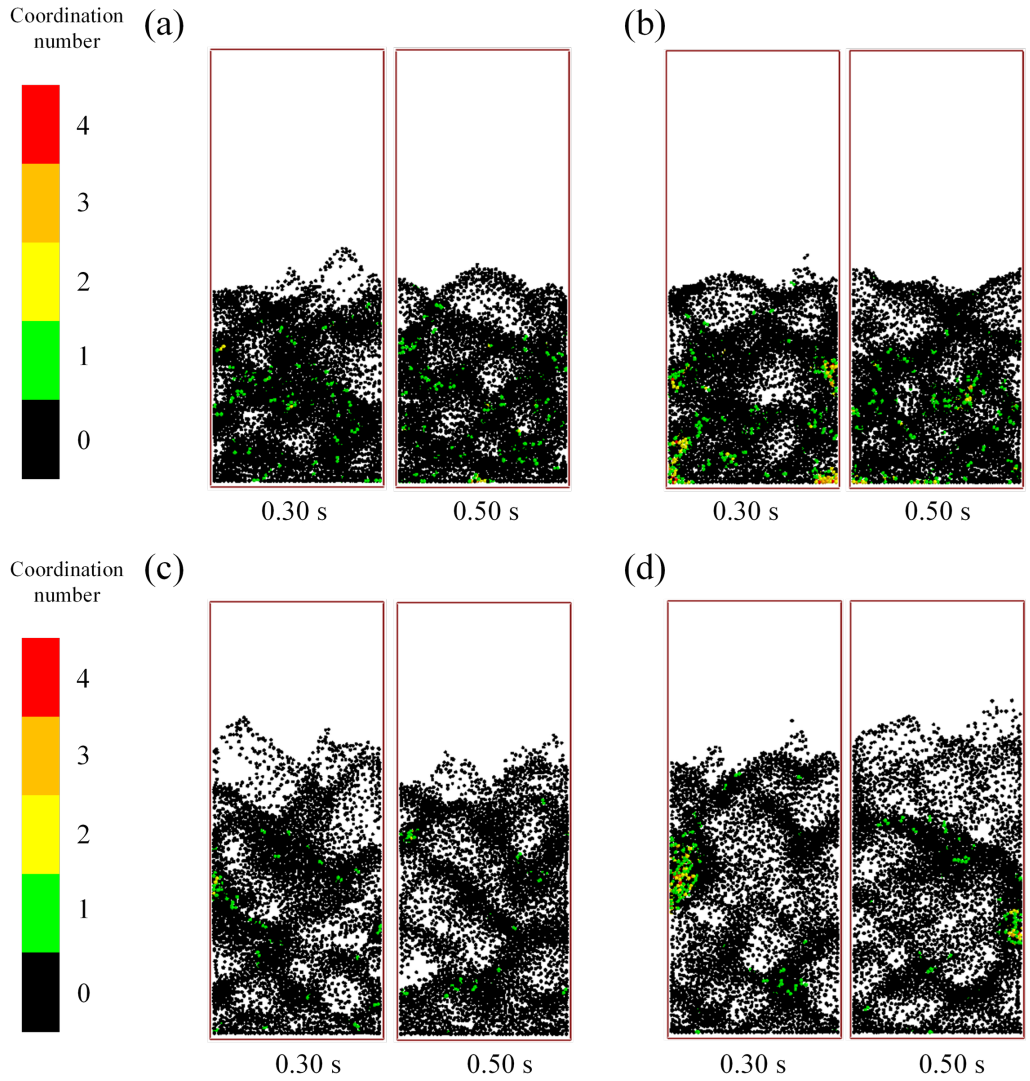


Figure 5. Instantaneous distributions of coordination number, (**a**) without VDW force, U = 0.012 m/s (**b**) with VDW force, U = 0.012 m/s (**c**) without VDW force, U = 0.020 m/s and (**d**) with VDW force, U = 0.020 m/s.

The spatial extent of elevated coordination number regions varies between snapshots. Figure 5b shows distinct regions of high contact density near the left wall at 0.30 s. Similarly, Figure 5d reveals a localized high contact density region near the left wall at 0.30 s. The results provide qualitative evidence of heterogeneous particle contacts. The localization of particle contacts is consistent with cohesion modifying the flow structure, as reported in simulations using adhesion force models. Elevated coordination number near the walls suggests preferential accumulation of contacting particles in the confined domain. It does not by itself demonstrate permanent particle–wall adhesion or wall sheeting, because coordination number measures particle–particle contacts. Changes in contact patterns indicate

that the interparticle connections change during fluidization. Gas driven rearrangement and cohesive attraction provide a plausible basis for this temporal variability.

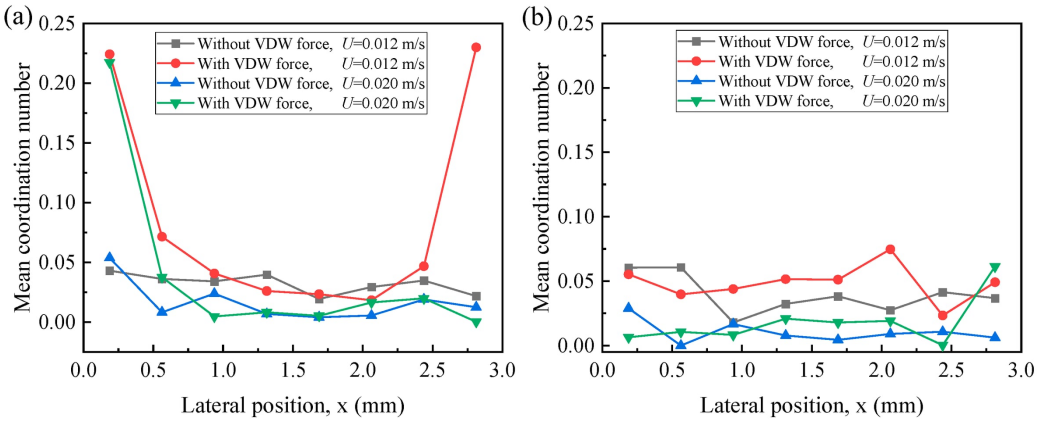


Figure 6. Mean coordination number profiles across the bed width at (**a**) 0.30 s and (**b**) 0.50 s.

Figure 6 quantitatively demonstrates the lateral redistribution of particle contacts. At 0.30 s, the cases with VDW forces exhibit pronounced near-wall peaks. At 0.012 m/s, the mean coordination numbers in the left and right wall sections reach 0.224 and 0.230, respectively, whereas the corresponding values without VDW forces remain 0.043 and 0.022. At 0.020 m/s, a similarly pronounced peak of approximately 0.217 appears near the left wall when VDW forces are included. In contrast, the cases without VDW forces exhibit lower and relatively uniform coordination number profiles across most of the bed width. At 0.50 s, the coordination number peaks become weaker and are redistributed spatially. For 0.012 m/s with VDW forces, the maximum shifts from the near wall regions to approximately 2.0625 mm. At 0.020 m/s, the VDW case develops a local peak near the right wall. These temporal changes indicate that the cohesive contact structures are dynamic rather than spatially fixed. Overall, VDW forces promote localized particle-contact networks, particularly near the walls, while the positions and magnitudes of these regions evolve because of the continuous formation, movement, and disruption of particle agglomerates. The near-wall coordination number peaks arise because wall confinement restricts lateral particle rearrangement, while cohesive attraction prolongs particle contacts after collision. The continuous competition between cohesive attraction and gas-driven particle separation causes these contact networks to form, move, and break over time.

Figure 7 shows the VDW force curves over 0.10–0.50 s. The plotted force is generally higher at 0.012 m/s than at 0.020 m/s. The curves exhibit time dependence. The lower velocity case exhibits repeated peaks, while the higher-velocity case has a lower baseline interrupted by intermittent peaks, including one near 0.31 s. Hence, the traces indicate sustained fluctuations rather than a monotonic approach to a constant force.

The lower plotted force at the higher gas velocity is consistent with a change in the particle configurations sampled during the fluidization process. In the VDW force model, the pair force depends on particle size, separation, and the Hamaker constant. Gas velocity can affect the recorded force through changes in particle positions and contacts, rather than by directly weakening the pair interaction at a fixed separation.

The repeated force peaks correspond to periods in which more particles approach one another closely or form cohesive contact networks, whereas the subsequent decreases reflect gas-driven particle separation and agglomerate disruption. The lower average force at 0.020 m/s therefore results from the shorter duration of close particle configurations rather than from a reduction in the pairwise VDW interaction at a given separation.

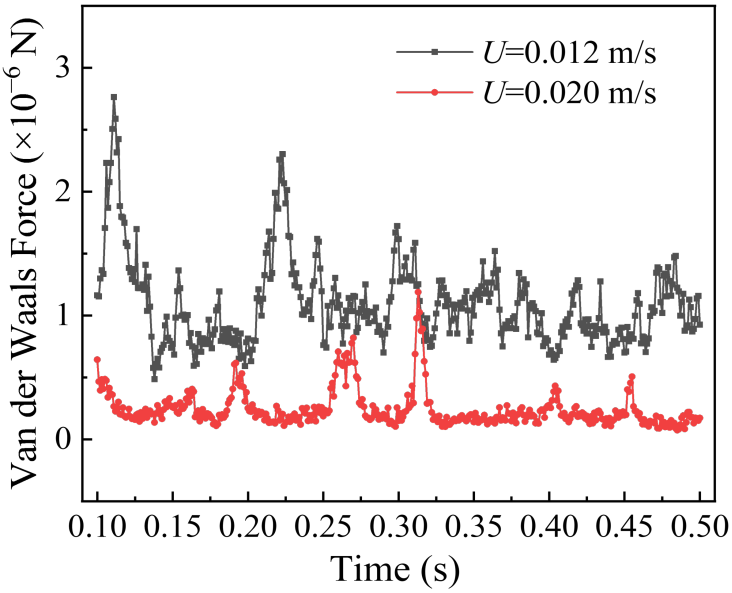


Figure 7. VDW force variation with time.

4.1.3. Particle Velocity

Figure 8 presents axial particle velocity as a function of the lateral coordinate x at heights z = 0.3, 1.5, 2.7, and 3.9 mm. Figure 8a,b show the cases at 0.012 m/s with and without VDW forces. Figure 8c,d show the corresponding cases at 0.020 m/s. Positive and negative values indicate upward and downward particle motion, respectively. At 0.012 m/s, the profiles are asymmetric, with both upward and downward motion at the three lower heights. The velocities at z = 3.9 mm are all negative. At 0.020 m/s, the largest plotted upward axial velocity decreases from approximately 0.016 m/s without VDW forces to 0.011 m/s with VDW forces. In the curve at z = 2.7 mm shown in Figure 8c, this extreme value occurs at an x value of 2.7 mm. In Figure 8d, this phenomenon occurs at x value of 1.5 mm and the same height. The change demonstrates a redistribution of axial particle motion.

The redistribution is particularly evident near the bed center at 0.020 m/s. Without VDW forces, the profiles in Figure 8c are negative at x value of 1.5 mm at all four heights. In contrast, the corresponding values in Figure 8d are positive at z = 1.5, 2.7, and 3.9 mm and close to zero at z = 0.3 mm. Upward velocities near x value of 2.7 mm remain present with VDW forces, but it is lower than those in the corresponding noncohesive case. Thus, the central upward motion region becomes more evident with VDW forces, while the effect remains asymmetric and height dependent. Considering the coordination-number distribution, these profiles suggest that changes in local particle connectivity and solids distribution influence particle transport. A larger change in the location of the dominant upward velocity is evident at 0.020 m/s, although the lower velocity profiles are also modified.

Figure 9 shows particle-velocity fields at three snapshots for each operating condition, with overlaid vectors. The particle configurations contain dense regions separated by particle poor voids, and the locations of the voids and high velocity regions vary between snapshots. The cases at 0.020 m/s exhibit a more expanded particle distribution than those at 0.012 m/s.

At 0.020 m/s, several of the most prominent high-velocity regions occur toward the sides of the bed without VDW forces in Figure 9c. As shown in Figure 9d, the positions of the points are closer to the center under the VDW forces. This qualitative pattern is consistent with the redistribution of axial particle velocity in Figure 8c,d. At 0.012 m/s, high velocity regions associated with particle-poor voids are visible in both Figure 9a,b.

The association between contact rich near wall regions shown in Figure 5 and the changes in particle motion shown in Figures 8 and 9 indicates that cohesion changes the spatial organization of the bed.

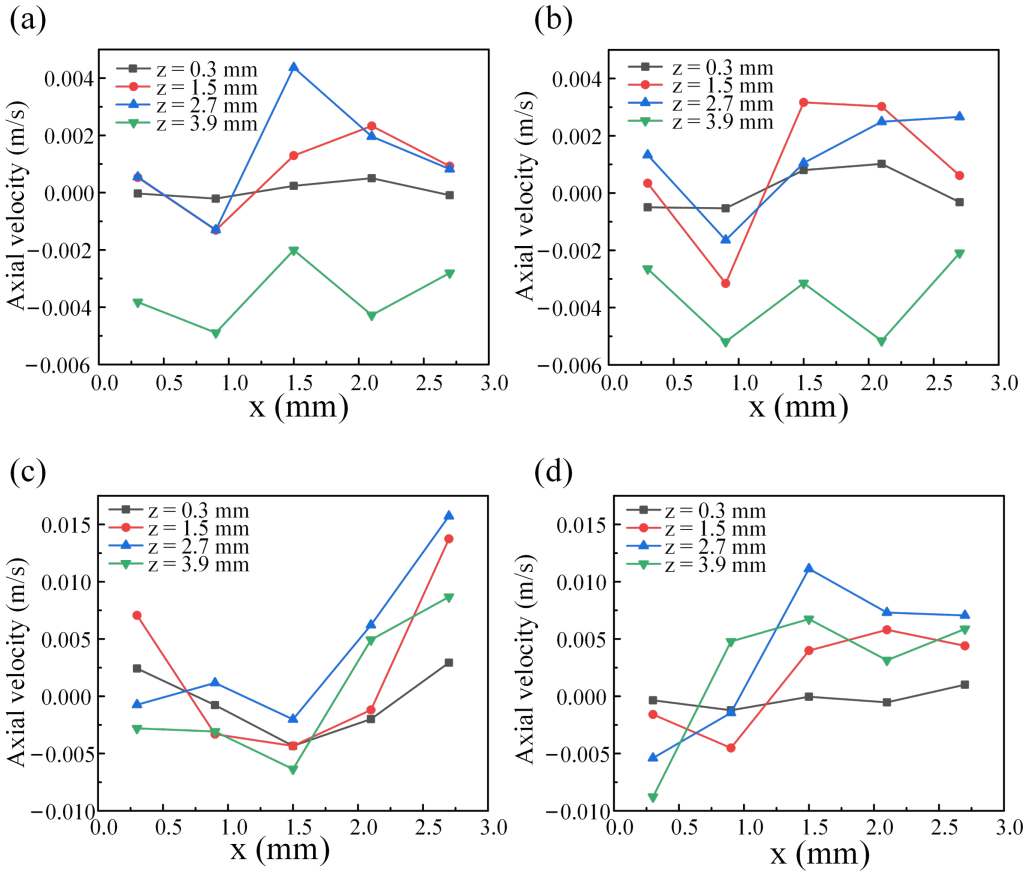


Figure 8. Particle-velocity distribution at different heights, (**a**) without VDW force, U = 0.012 m/s (**b**) with VDW force, U = 0.012 m/s (**c**) without VDW force, U = 0.020 m/s and (**d**) with VDW force, U = 0.020 m/s.

4.1.4. Bed-Pressure Drop

Figure 10 presents the temporal evolution of the bed-pressure drop under the four operating conditions. Immediately after gas injection, the pressure drop decreases rapidly from its initial peak as the initially packed particle bed expands and reorganizes. It subsequently fluctuates around an approximately constant mean. Using a 0.05-s moving average, the onset of the quasi-steady regime is defined as the first time at which the moving-average pressure drop enters within ±5% of its terminal plateau and remains within this range for at least 0.05 s. The corresponding stabilization times are approximately 0.092 and 0.116 s for the cases without and with VDW forces at 0.012 m/s, respectively, and 0.133 and 0.157 s at 0.020 m/s. Therefore, t $\geq$ 0.16 s is selected as the common quasi-steady averaging interval. During this interval, the mean pressure drops without and with VDW forces are 25.45 $\pm$ 0.97 and 25.30 $\pm$ 0.88 Pa at 0.012 m/s, and 22.65 $\pm$ 1.40 and 22.77 $\pm$ 1.93 Pa at 0.020 m/s, respectively. The uncertainties represent temporal standard deviations. The pressure drop fluctuations are comparable for the two cases at 0.012 m/s, whereas the standard deviation increased when VDW forces are included at 0.020 m/s. This increased fluctuation is consistent with the repeated formation and disruption of cohesive particle structures under stronger gas-particle forcing.

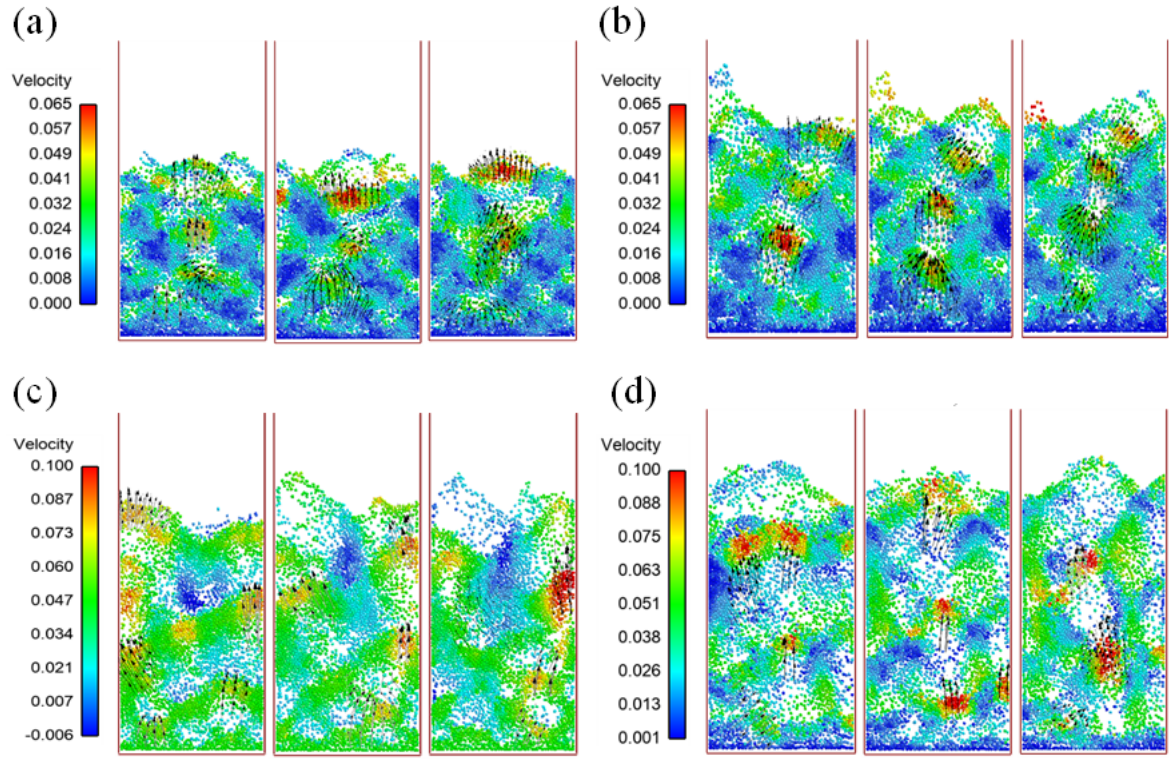


Figure 9. Distribution of particle velocity with time, (**a**) without VDW force, U = 0.012 m/s (**b**) with VDW force, U = 0.012 m/s (**c**) without VDW force, U = 0.020 m/s and (**d**) with VDW force, U = 0.020 m/s.

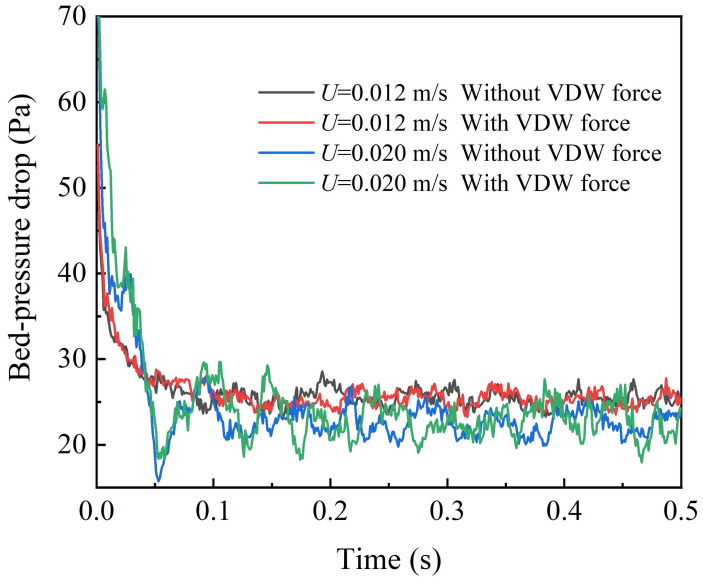


Figure 10. Pressure-drop variation over time.

4.2. Heat-Transfer Characteristics

4.2.1. Gas Temperature

Figure 11 presents the axial gas temperature profiles. Gas enters at 313 K and is heated through exchange with particles at an initial temperature of 361 K. These four curves all rise sharply near the inlet and approach approximately 361 K at a height of 0.0008 m. Therefore, the main temperature change occurs within a short entrance region. Above this region, the temperature distribution curves are nearly identical. The heating is driven by the gas-particle temperature difference. The specified operating pressure is not itself a heat

source. When the velocity is 0.012 m/s, the curve representing the VDW forces initially lies below the curve representing the case without VDW forces. The two curves then approach each other and cross at several points. At 0.020 m/s, the gas temperature is higher with VDW forces than without VDW forces. Consequently, VDW forces do not uniformly accelerate gas heating at both velocities. The different curves are consistent with changes in local particle distribution and gas transport, while the downstream temperatures are nearly identical, indicating a limited influence on the overall axial-temperature profile.

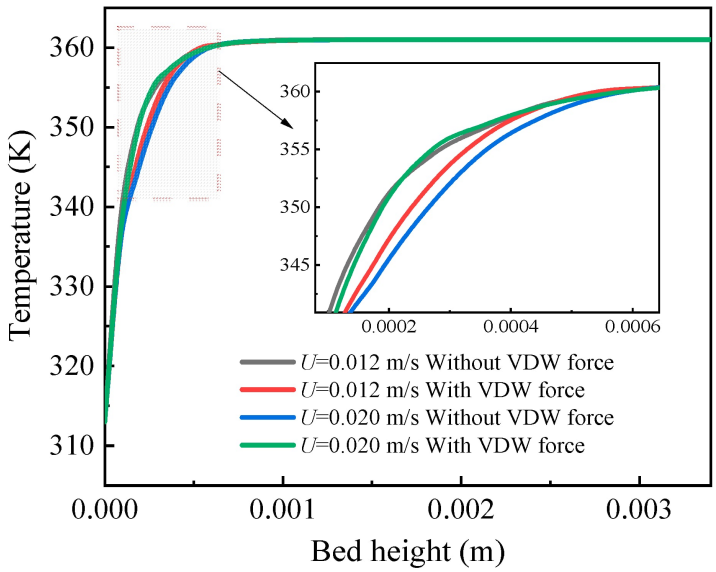


Figure 11. Variation of temperature along the bed height.

4.2.2. Heat-Transfer Coefficient

Particle-to-particle conduction and particle-to-gas convection are two distinct heat-transfer mechanisms. The heat-transfer coefficient specifically denotes the particle-to-gas convective coefficient. Figure 12 compares the instantaneous particle-ensemble-averaged heat-transfer coefficients at 0.18 and 0.35 s. Both instants occur after the onset of the quasi-steady pressure-drop regime. At each instant, the coefficient is spatially averaged over all particles in the bed. These values characterize the instantaneous thermal response of the particle ensemble. The effect of VDW forces is evaluated by comparing the cases with and without VDW forces at the same gas velocity and time. At 0.012 m/s, relative to the cases without VDW forces, the inclusion of VDW forces increases the coefficient by 0.87% at 0.18 s and 0.93% at 0.35 s. At 0.020 m/s, the inclusion of VDW forces increases the coefficient by 6.12% at 0.18 s and 6.03% at 0.35 s. The VDW-related enhancement is therefore consistently less than 1% at 0.012 m/s but approximately 6% at 0.020 m/s at both quasi-steady instants. This comparison indicates that the influence of VDW forces on particle-to-gas convective heat transfer becomes more pronounced at the higher gas velocity.

The different responses at the two gas velocities can be explained by the coupling between agglomerate dynamics and local gas-particle hydrodynamics. The coordination number characterizes the connectivity of the particle contact network. However, it does not directly determine the particle-to-gas convective heat-transfer coefficient. The coefficient depends on the local gas volume fraction and gas–particle relative velocity through the particle Reynolds number and Nusselt number. Therefore, a higher coordination number does not necessarily produce a proportionally higher convective heat transfer coefficient.

At 0.012 m/s, VDW forces prolong particle contacts, but the resulting changes in local voidage and gas-particle slip velocity remain limited. Consequently, the increase in the convective heat-transfer coefficient is less than 1%. At 0.020 m/s, stronger gas forcing

promotes repeated formation, deformation, and disruption of cohesive particle structures. This dynamic process produces greater redistribution of local voidage and gas-particle slip velocity, increasing by approximately 6%. Thus, the convective heat-transfer response is governed not only by particle-contact connectivity but also by the dynamic agglomerate structure and its influence on the surrounding gas flow.

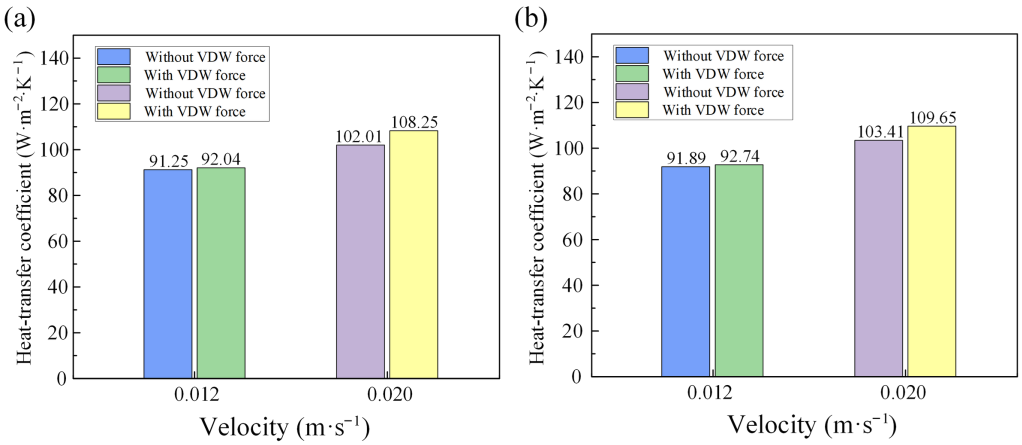


Figure 12. Average heat-transfer coefficient at different times (**a**) 0.18 s (**b**) 0.35 s.

5. Conclusions

A coupled CF-DDEM model incorporating VDW forces and heat transfer is employed to investigate the hydrodynamic and heat-transfer characteristics of fine polyethylene particles in a fluidized bed reactor under high temperature and high pressure. The main conclusions are as follows:

(1) VDW forces modify the local gas–solid structure and enhance particle connectivity, with elevated coordination number regions occurring particularly near the sidewalls and bottom corners. The recorded VDW forces are generally higher at 0.012 m/s, indicating that gas velocity influences the realized cohesive interactions by altering particle configurations and contacts.

(2) VDW forces redistribute particle motion, and their macroscopic influence becomes more evident at the higher gas velocity. At 0.020 m/s, the maximum upward particle velocity decreases and the dominant upward motion region shifts toward the bed center when VDW forces are included, demonstrating a pronounced redistribution of particle transport.

(3) VDW forces have a limited effect on the axial gas-temperature distribution but a more pronounced influence on the particle-to-gas convective heat-transfer coefficient. This difference occurs because VDW forces modify the local voidage and gas-particle relative velocity. The gas rapidly approaches the particle temperature near the inlet, substantially reducing the downstream thermal driving force. At 0.020 m/s, VDW forces increase the average convective heat-transfer coefficient by approximately 6.12% at 0.18 s.

However, the simulations are conducted in a small and simplified computational domain over a limited range of operating conditions. Therefore, the reported results should be interpreted as mechanistic observations rather than direct quantitative predictions for industrial-scale fluidized bed reactors. Further studies using larger three-dimensional domains, longer simulation periods, and additional operating conditions are required before the model can be applied quantitatively to industrial reactor design and scale-up.

Author Contributions: L.W.: Investigation, data curation, writing—original draft, funding acquisition. J.L.: Investigation, conceptualization, supervision, writing—review and editing. H.Q.: Project administration, writing—reviewing and editing. All authors have read and agreed to the published version of the manuscript.

Funding: This research was funded by the financial support from the Science and Technology Development Plan Project of Jilin Province, China, grant number YDZJ202601ZYTS190.

Data Availability Statement: The original contributions presented in this study are included in the article. Further inquiries can be directed to the corresponding author.

Conflicts of Interest: The authors declare that they have no known competing financial interests or personal relationships that could have appeared to influence the work reported in this paper.

References

1. Duan, Y.; Li, L.; Lu, D.; Zhang, S.; Sun, G.; Sun, Z.; Duan, L. Innovative approaches to carbon capture using fluidized bed reactors: A brief review. *Fuel* **2026**, *414*, 138295. [CrossRef]
2. Lei, H.; Zhu, L.-T.; Yang, Y.-N.; Luo, Z.-H. A CFD-DEM study of regulating heat transfer and reaction performance in liquid-injected polymerization fluidized beds. *Chem. Eng. Sci.* **2026**, *328*, 123749. [CrossRef]
3. Nimvari, M.I.; Sowinski, A.; Mehrani, P. Contact electrification of a live metallocene catalyst and its components in an atmospheric polyethylene fluidized bed. *Chem. Eng. J.* **2025**, *517*, 164472. [CrossRef]
4. Marchelli, F.; Fiori, L.; Di Felice, R. Cohesive particle-fluid systems: An overview of their CFD simulation. *Can. J. Chem. Eng.* **2025**, *103*, 1582–1601. [CrossRef]
5. Zhang, S.; Zhao, L.; Feng, J.; Dong, H. Numerical investigation of the air-particles heat transfer characteristics of moving bed-effect of particle size distribution. *Int. J. Heat Mass Transf.* **2022**, *182*, 122036. [CrossRef]
6. Che, Y.; Tian, Z.; Liu, Z.; Zhang, R.; Gao, Y.; Zou, E.; Wang, S.; Liu, B. CFD prediction of scale-up effect on the hydrodynamic behaviors of a pilot-plant fluidized bed reactor and preliminary exploration of its application for non-pelletizing polyethylene process. *Powder Technol.* **2015**, *278*, 94–110. [CrossRef]
7. Ghasem, N. Transient behavior and control of polyethylene production in a fluidized bed reactor utilizing population balance model. *Int. J. Mol. Sci.* **2024**, *25*, 2602. [CrossRef] [PubMed]
8. Hadadiyan, M.; Mostoufi, N.; Marandi, R. Particle size distribution in a multi-zone circulating fluidized bed polymerization reactor. *Particuology* **2024**, *93*, 291–299. [CrossRef]
9. Kulajanpeng, K.; Sheibat-Othman, N.; Tanthapanichakoon, W.; McKenna, T.F.L. Modeling of a multizone circulating reactor for gas-phase propylene (co)polymerization: From pilot to full scale reactors. *Ind. Eng. Chem. Res.* **2025**, *64*, 7264–7282. [CrossRef]
10. Ashrafi, O.; Mostoufi, N.; Sotudeh-Gharebagh, R. Two phase steady-state particle size distribution in a gas-phase fluidized bed ethylene polymerization reactor. *Chem. Eng. Sci.* **2012**, *73*, 1–7. [CrossRef]
11. Kim, J.Y.; Choi, K.Y. Modeling of particle segregation phenomena in a gas phase fluidized bed olefin polymerization reactor. *Chem. Eng. Sci.* **2001**, *56*, 4069–4083. [CrossRef]
12. Che, Y.; Tian, Z.; Liu, Z.; Zhang, R.; Gao, Y.; Zou, E.; Wang, S.; Liu, B. A CFD-PBM model considering ethylene polymerization for the flow behaviors and particle size distribution of polyethylene in a pilot-plant fluidized bed reactor. *Powder Technol.* **2015**, *286*, 107–123. [CrossRef]
13. Schneiderbauer, S.; Pirker, S.; Puttinger, S.; Aguayo, P.; Touloupidis, V.; Martínez Joaristi, A. A Lagrangian-Eulerian hybrid model for the simulation of poly-disperse fluidized beds: Application to industrial-scale olefin polymerization. *Powder Technol.* **2017**, *316*, 697–710. [CrossRef]
14. Pan, H.; Liu, Q.; Luo, Z.-H. Modeling and simulation of particle size distribution behavior in gas-liquid-solid polyethylene fluidized bed reactors. *Powder Technol.* **2018**, *328*, 95–107. [CrossRef]
15. Syed, T.M.; Mehrani, P. Influence of argon gas composition and temperature on the extent of wall fouling due to static charge in a pressurized gas-solid fluidized bed. *Powder Technol.* **2026**, *482*, 122796. [CrossRef]
16. Rokkam, R.G.; Fox, R.O.; Muhle, M.E. Computational fluid dynamics and electrostatic modeling of polymerization fluidized-bed reactors. *Powder Technol.* **2010**, *203*, 109–124. [CrossRef]
17. Song, D.; Mehrani, P. Mechanism of particle build-up on gas-solid fluidization column wall due to electrostatic charge generation. *Powder Technol.* **2017**, *316*, 166–170. [CrossRef]
18. Yang, Y.; Zi, C.; Huang, Z.; Wang, J.; Lungu, M.; Liao, Z.; Yang, Y.; Su, H. CFD-DEM investigation of particle elutriation with electrostatic effects in gas-solid fluidized beds. *Powder Technol.* **2017**, *308*, 422–433. [CrossRef]
19. Hadisarabi, M.; Gharebagh, R.S.; Zarghami, R.; Mostoufi, N. Computational modeling of the electrostatic charge build-up in fluidized beds. *J. Electrost.* **2019**, *97*, 108–120. [CrossRef]
20. Briens, C.L.; Bergougnou, M.A.; Inculet, I.I.; Baron, T.; Hazlett, J.D. Size distribution of particles entrained from fluidized beds: Electrostatic effects. *Powder Technol.* **1992**, *70*, 57–62. [CrossRef]
21. Zhang, P.; Liang, C.; Zhou, Q.; Chen, X.; Ma, J. Experimental investigation of particle adhesion on the wall due to electrostatic charge in gas-solid fluidized beds. *Powder Technol.* **2021**, *387*, 373–384. [CrossRef]

22. Jiang, P.; Bi, H.; Liang, S.-C.; Fan, L.-S. Hydrodynamic behavior of circulating fluidized bed with polymeric particles. *AIChE J.* **1994**, *40*, 193–206. [CrossRef]
23. Visser, J. Van der Waals and other cohesive forces affecting powder fluidization. *Powder Technol.* **1989**, *58*, 1–10. [CrossRef]
24. Li, T.; Rabha, S.; Verma, V.; Dietiker, J.-F.; Xu, Y.; Lu, L.; Rogers, W.; Gopalan, B.; Breault, G.; Tucker, J.; et al. Experimental study and discrete element method simulation of Geldart Group A particles in a small-scale fluidized bed. *Adv. Powder Technol.* **2017**, *28*, 2961–2973. [CrossRef]
25. Shrestha, S.; Kuang, S.B.; Yu, A.B.; Zhou, Z.Y. Effect of van der Waals force on bubble dynamics in bubbling fluidized beds of ellipsoidal particles. *Chem. Eng. Sci.* **2020**, *212*, 115343. [CrossRef]
26. Gu, Y.; Ozel, A.; Sundaresan, S. A modified cohesion model for CFD-DEM simulations of fluidization. *Powder Technol.* **2016**, *296*, 17–28. [CrossRef]
27. Mihajlovic, M.; Roghair, I.; Van Sint Annaland, M. On the numerical implementation of the van der Waals force in soft-sphere discrete element models for gas-solid fluidization. *Chem. Eng. Sci.* **2020**, *226*, 115794. [CrossRef]
28. Bellan, S.; Matsubara, K.; Cho, H.S.; Gokon, N.; Kodama, T. A CFD-DEM study of hydrodynamics with heat transfer in a gas-solid fluidized bed reactor for solar thermal applications. *Int. J. Heat Mass Transf.* **2018**, *116*, 377–392. [CrossRef]
29. Li, H.-W.; Wang, L.; Wang, T.; Du, C.-H. Experimental and CFD-DEM numerical evaluation of flow and heat transfer characteristics in mixed pulsed fluidized beds. *Adv. Powder Technol.* **2020**, *31*, 3144–3157. [CrossRef]
30. Hamaker, H.C. The London-van der Waals attraction between spherical particles. *Physica* **1937**, *4*, 1058–1072. [CrossRef]
31. Gan, J.Q.; Zhou, Z.Y.; Yu, A.B. Micromechanical analysis of flow behaviour of fine ellipsoids in gas fluidization. *Chem. Eng. Sci.* **2017**, *163*, 11–26. [CrossRef]
32. Aarons, L.; Sundaresan, S. Shear flow of assemblies of cohesive and non-cohesive granular materials. *Powder Technol.* **2006**, *169*, 10–21. [CrossRef]
33. Zhang, K.; Wang, S.; Li, B.; He, Y.; Zhao, Y. Heat transfer in a pulsed fluidized bed by using coupled CFD-DEM method. *Powder Technol.* **2020**, *367*, 497–505. [CrossRef]
34. Zbib, H.; Ebrahimi, M.; Ein-Mozaffari, F.; Lohi, A. Comprehensive analysis of fluid-particle and particle-particle interactions in a liquid-solid fluidized bed via CFD-DEM coupling and tomography. *Powder Technol.* **2018**, *340*, 116–130. [CrossRef]
35. Ebrahimi, M.; Crapper, M. CFD-DEM simulation of turbulence modulation in horizontal pneumatic conveying. *Particuology* **2017**, *31*, 15–24. [CrossRef]
36. Geng, Y.; Che, D. An extended DEM-CFD model for char combustion in a bubbling fluidized bed combustor of inert sand. *Chem. Eng. Sci.* **2011**, *66*, 207–219. [CrossRef]
37. Fattahi, M.; Hosseini, S.H.; Ahmadi, G.; Parvareh, A. Numerical simulation of heat transfer coefficient around different immersed bodies in a fluidized bed containing Geldart B particles. *Int. J. Heat Mass Transf.* **2019**, *141*, 353–366. [CrossRef]
38. Chilamkurti, Y.N.; Gould, R.D. CFD-DEM and PR-DNS studies of low-temperature densely packed beds. *Int. J. Heat Mass Transf.* **2020**, *159*, 120056. [CrossRef]
39. Geldart, D. Types of gas fluidization. *Powder Technol.* **1973**, *7*, 285–292. [CrossRef]
40. Shabanian, J.; Chaouki, J. Hydrodynamics of a gas-solid fluidized bed with thermally induced interparticle forces. *Chem. Eng. J.* **2015**, *259*, 135–152. [CrossRef]
41. Badran, Y.; Ansart, R.; Chaouki, J.; Simonin, O. Macro-scale numerical investigation of the contribution of van der Waals force to the pressure-drop overshoot in fine-particle fluidized beds. *Powder Technol.* **2024**, *436*, 119505. [CrossRef]
42. Che, Y.; Tian, Z.; Zhang, R.; Gao, Y.; Zou, E.; Wang, S.; Liu, B. 3D numerical simulation of flow characteristics for Geldart B and Geldart D particles in gas phase ethylene polymerization fluidized-bed reactor. *CIESC J.* **2016**, *67*, 519–529.
43. LaMarche, C.Q.; Liu, P.; Kellogg, K.M.; Hrenya, C.M. Fluidized-bed measurements of carefully-characterized, mildly-cohesive (Group A) particles. *Chem. Eng. J.* **2017**, *310*, 259–271. [CrossRef]

Disclaimer/Publisher's Note: The statements, opinions and data contained in all publications are solely those of the individual author(s) and contributor(s) and not of MDPI and/or the editor(s). MDPI and/or the editor(s) disclaim responsibility for any injury to people or property resulting from any ideas, methods, instructions or products referred to in the content.